

Dirac mass generation from crystal symmetry breaking on the surfaces of topological crystalline insulators

Ilija Zeljkovic^{1†}, Yoshinori Okada^{1,2†}, Maksym Serbyn^{3,4}, R. Sankar^{5,6}, Daniel Walkup¹, Wenwen Zhou¹, Junwei Liu³, Guoqing Chang⁷, Yung Jui Wang⁸, M. Zahid Hasan⁹, Fangcheng Chou⁵, Hsin Lin⁷, Arun Bansil⁸, Liang Fu³ and Vidya Madhavan^{1,10*}

The tunability of topological surface states and controllable opening of the Dirac gap are of fundamental and practical interest in the field of topological materials. In the newly discovered topological crystalline insulators (TCIs), theory predicts that the Dirac node is protected by a crystalline symmetry and that the surface state electrons can acquire a mass if this symmetry is broken. Recent studies have detected signatures of a spontaneously generated Dirac gap in TCIs; however, the mechanism of mass formation remains elusive. In this work, we present scanning tunnelling microscopy (STM) measurements of the TCI $\text{Pb}_{1-x}\text{Sn}_x\text{Se}$ for a wide range of alloy compositions spanning the topological and non-topological regimes. The STM topographies reveal a symmetry-breaking distortion on the surface, which imparts mass to the otherwise massless Dirac electrons—a mechanism analogous to the long sought-after Higgs mechanism in particle physics. Interestingly, the measured Dirac gap decreases on approaching the trivial phase, whereas the magnitude of the distortion remains nearly constant. Our data and calculations reveal that the penetration depth of Dirac surface states controls the magnitude of the Dirac mass. At the limit of the critical composition, the penetration depth is predicted to go to infinity, resulting in zero mass, consistent with our measurements. Finally, we discover the existence of surface states in the non-topological regime, which have the characteristics of gapped, double-branched Dirac fermions and could be exploited in realizing superconductivity in these materials.

Topological crystalline insulators¹ represent a new class of topologically non-trivial materials hosting Dirac surface states (SS) with distinct characteristics^{2–4}. Similar to conventional Z_2 topological insulators (TIs^{5–9}), the Dirac states in TCIs develop in response to an inverted bulk gap caused by strong spin–orbit coupling. However, unlike conventional TIs^{10–12}, the SS are located away from the time-reversal invariant points in the Brillouin zone and are therefore not protected by time-reversal symmetry. Instead, the Dirac nodes in TCIs are protected by structural crystalline symmetries². The resulting Chern number of ± 2 allows an even number of Dirac nodes within the Brillouin zone. Correspondingly, the topological SS in the (001) plane of the TCI $\text{Pb}_{1-x}\text{Sn}_x\text{Se}$ consist of two pairs of Dirac nodes, located in the vicinity of the \bar{X} and \bar{Y} points in the two-dimensional surface Brillouin zone, with each pair of Dirac nodes protected by its respective mirror symmetry plane¹. The defining characteristic of TCIs is that as long as mirror symmetries are preserved, that is, the crystal structure is cubic, the Dirac nodes should remain gapless and the material should host massless Dirac fermions. The smoking-gun experiment to prove this protection would be to break the mirror symmetry and create a gap. Landau level (LL) spectroscopy of $\text{Pb}_{1-x}\text{Sn}_x\text{Se}$ (ref. 3) suggests that, in one of the

two mirror directions, mirror symmetry is spontaneously broken, thereby providing mass to one pair of Dirac nodes while leaving the other pair massless¹³. So far, however, the structural distortion postulated to do this has not been observed.

In this work, we use scanning tunnelling microscopy and spectroscopy (STM/S) to track the evolution of the SS in a TCI^{1,2}, $\text{Pb}_{1-x}\text{Sn}_x\text{Se}$ (ref. 14), that can be tuned continuously by changing the alloy composition (x) from the topological to the trivial phase¹⁵. By obtaining high-resolution topographies of the surface structure, we discover a crystal distortion that breaks mirror symmetry for only one of the two mirror planes. Simultaneous measurements of Landau levels show the corresponding acquisition of mass in one direction. Our experiments provide the first direct proof that the Dirac node is protected by mirror symmetry in this new class of topological materials. Furthermore, through LL spectroscopy^{16–19}, we track the evolution of the mass and the distortion across the phase diagram. Surprisingly, we find that whereas the mass decreases monotonically as we approach the phase transition, vanishing at the critical point (x_c), the magnitude of the distortion remains relatively unchanged. This is inconsistent with a simple picture in which the changing mass originates from a varying distortion. Instead, our observations can be explained by the

¹Department of Physics, Boston College, Chestnut Hill, Massachusetts 02467, USA. ²WPI-AIMR, Tohoku University, Sendai 980-8577, Japan.

³Massachusetts Institute of Technology, Cambridge, Massachusetts 02139, USA. ⁴Department of Physics, University of California, Berkeley, California

94720-7300, USA. ⁵Center for Condensed Matter Sciences, National Taiwan University, Taipei 10617, Taiwan. ⁶Institute of Physics, Academia Sinica,

Taipei 11529, Taiwan. ⁷Graphene Research Centre and Department of Physics, National University of Singapore, Singapore 117542, Singapore. ⁸Department

of Physics, Northeastern University, Boston, Massachusetts 02115, USA. ⁹Joseph Henry Laboratory, Department of Physics, Princeton University,

Princeton, New Jersey 08544, USA. ¹⁰Department of Physics and Frederick Seitz Materials Research Laboratory, University of Illinois Urbana-Champaign,

Urbana, Illinois 61801, USA. [†]These authors contributed equally to this work. *e-mail: vm1@illinois.edu

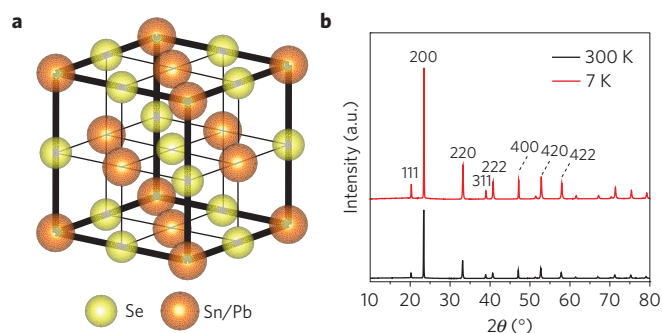


Figure 1 | Bulk cubic crystal structure of $\text{Pb}_{1-x}\text{Sn}_x\text{Se}$. **a**, Schematic of the face-centred cubic crystal structure, showing the Se and Pb/Sn sublattices. **b**, X-ray diffraction intensity data for $x \sim 0.35$, showing a single phase cubic crystal structure without detectable symmetry breaking as a result of Sn substitution detected both at room temperature (black) and 7 K (red).

increasing penetration of the SS into the bulk as we approach x_c . In this scenario, the distortion observed in STM is restricted to the surface. The magnitude of the mass is therefore controlled by the weight of the SS at the topmost layer, which decreases with increasing bulk penetration of the SS. Our results thus present direct experimental evidence in support of the theoretical picture of the fate of the SS electrons close to the critical composition where the trivial state is achieved via complete penetration of the bulk of the sample by the Dirac electrons. Finally, on the trivial side, we make a surprising discovery of novel remnant SS, which exhibit many of the characteristics of their topological counterparts.

$\text{Pb}_{1-x}\text{Sn}_x\text{Se}$ single crystals in the range of Sn concentrations studied in this work are expected to have a face-centred cubic structure²⁰ (Fig. 1). From the square atomic lattice seen in the low-bias STM topographs (Fig. 2c,d), the crystals cleave along the (001) direction, exposing one of the two sublattices. To explore the evolution of the SS on the (001) face, we perform LL spectroscopy in a magnetic field on a series of samples spanning the quantum phase transition from the trivial to the topological phase: $x \sim 0.09$ (trivial), 0.17 (critical), 0.29 (topological) and 0.34 (topological) (Fig. 3). Our first task is to ascertain the existence of Dirac SS in the topological samples. To accomplish this, we determine the presence of the Dirac nodes at different Sn concentrations across the transition point (Fig. 3). The Dirac node signifies the continuous nature of the topological SS bands, which necessarily span the gap between the conduction and valance bands. The presence of this topologically protected point is manifested as a non-dispersing (energy independent of magnetic field) zeroth LL peak in dI/dV spectra located near the minimum. We find that such a non-dispersing peak is seen clearly in all three non-trivial samples (Fig. 3f–h). In contrast, although LLs signifying the existence of SS are clearly observed even in the trivial $x \sim 0.09$ sample (Fig. 3e), the zeroth LL is notably absent, indicating the non-topological nature of the SS.

In the topological samples, we find two additional non-dispersing peaks, labelled E_+^* and E_-^* (Fig. 3c,d,g,h) on either side of the zeroth LL peak. The non-dispersing nature and the coexistence of the E^* peaks with the peak at the Dirac point suggest that the E^* peaks correspond to mass acquisition in two out of the four Dirac cones within the first Brillouin zone (Fig. 4a)³. The resulting mass energy scale can be characterized by the mass gap $\Delta = |E_+^* - E_-^*|$. Interestingly, we find that Δ decreases monotonically from ~ 24.2 meV for $x \sim 0.38$ to ~ 0 meV near the critical doping of

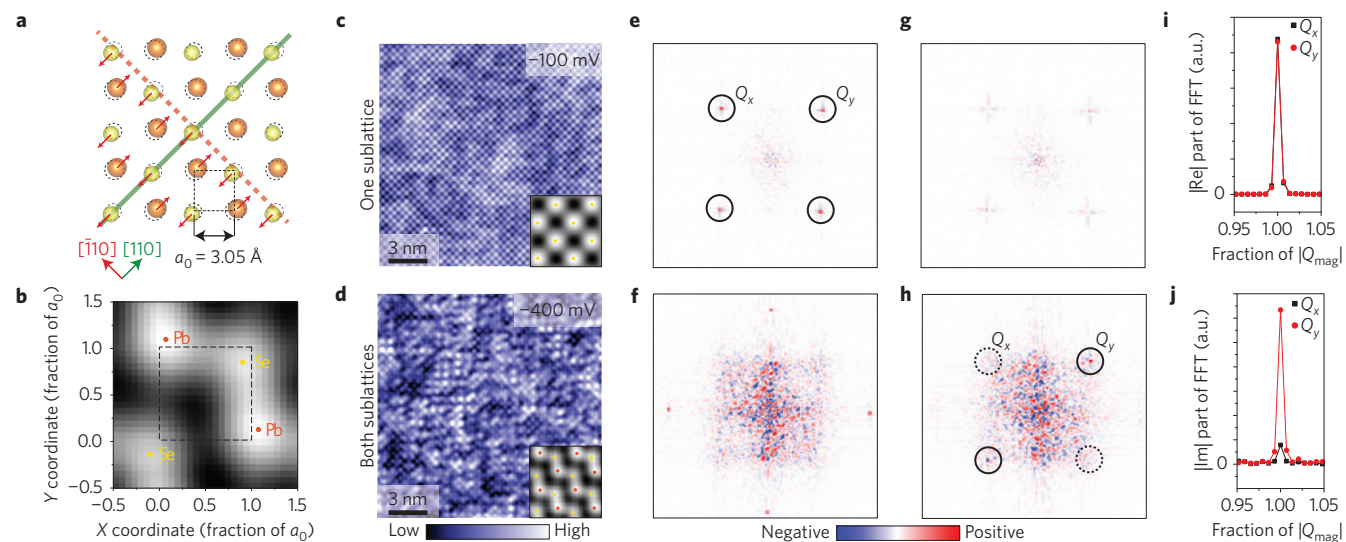


Figure 2 | Symmetry-breaking distortion on the surface of $\text{Pb}_{1-x}\text{Sn}_x\text{Se}$. **a**, Schematic representation of the distortion in the surface layer. Two sublattices shift in opposite manners along the [110] direction, as denoted by red arrows. Even though [110] mirror symmetry is still preserved (green line), the distortion breaks $\bar{1}10$ mirror symmetry (dashed red line). Dashed black circles represent the ideal atomic positions in a cubic lattice without the distortion. **b**, Average 2×2 -atom supercell obtained from the experimental topograph in **d**. The centres of average atoms determined by Gaussian fitting are denoted by yellow and orange dots, and the dashed square represents the tetragonal unit cell in the absence of distortion (see Supplementary Discussion I for more details). **c,d**, STM topographs of the $x \sim 0.38$ sample showing only the Se sublattice (**c**; see Supplementary Discussion II) and both sublattices (**d**) acquired over the same area of the sample. Insets in **c,d** show a 4×4 -atom supercell aligned along the atomic Bragg peak directions²⁴. Yellow and orange dots represent the centres of Se and Pb/Sn atoms, respectively. **e,f**, Real part of the Fourier transform of the STM topographs in **c,d**, respectively. **g,h**, Imaginary part of the Fourier transform of STM topographs in **c,d**, respectively. **i**, Line cut starting from the centre of the Fourier transform in **e** through the atomic Bragg peaks Q_x and Q_y , showing the C_4 symmetry of our STM tip. **j**, Line cut starting from the centre of the Fourier transform in **h** through the atomic Bragg peaks Q_x and Q_y , showing the symmetry-breaking distortion present along only the Q_y direction. STM set-up conditions are: $I_{\text{set}} = 200$ pA, $V_{\text{set}} = -100$ mV (**c**); $I_{\text{set}} = 900$ pA, $V_{\text{set}} = -400$ mV (**d**).

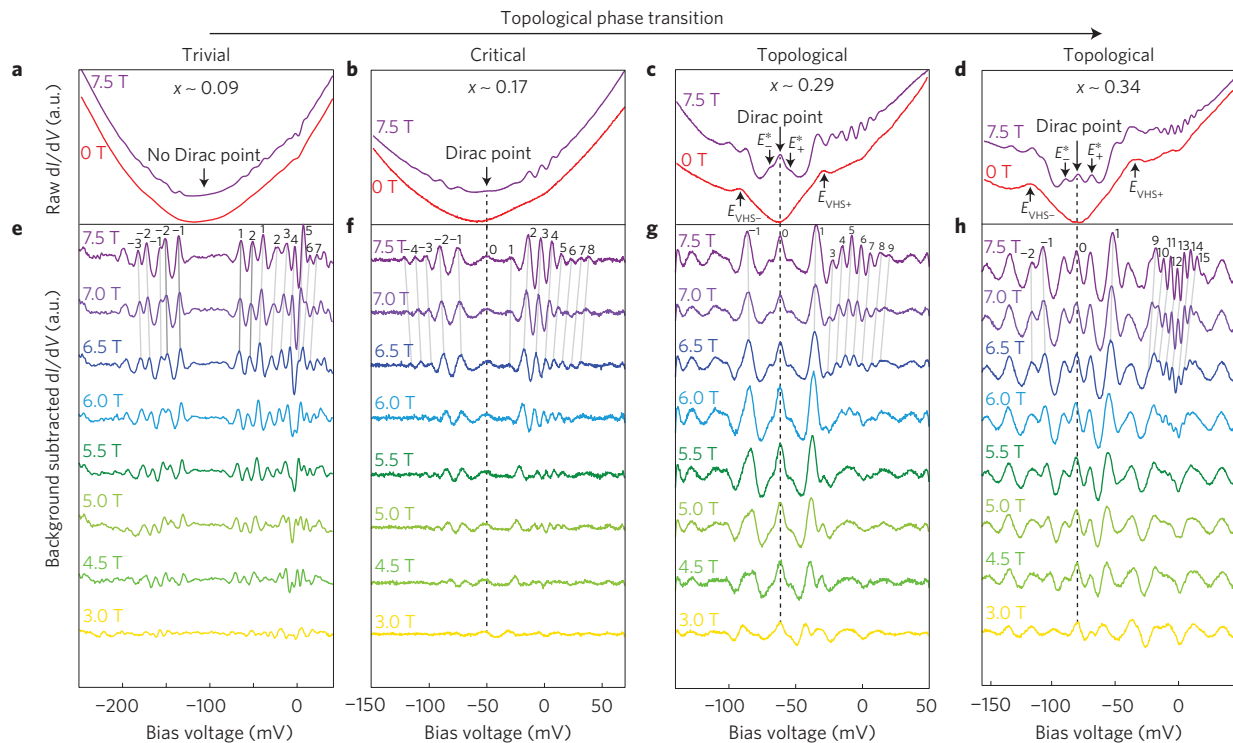


Figure 3 | Landau level spectroscopy. **a–d**, Average dI/dV curves acquired at magnetic fields of 0 T and 7.5 T over the same area of the sample for Sn fractions $x \sim 0.09$, 0.17, 0.29 and 0.34 Sn, respectively. **e–h**, Waterfall plots of background subtracted dI/dV curves (see Supplementary Discussion III for normalization details) acquired as a function of magnetic field, showing LLs as prominent dispersing ripples. Indexing of LLs used to plot the dispersions in Fig. 6 is denoted in each panel. No Dirac point is present in the trivial sample (**e**), whereas a prominent non-dispersing peak that develops under application of a magnetic field signals the Dirac node formation in **f–h**. Other non-dispersing peaks in **c,d,g,h**, labelled as E_{\pm}^* and E_{\pm}^* , indicate the presence of massive Dirac fermions³. E_{VHS+} and E_{VHS-} denote the positions of two van Hove singularities, which are directly related to the two Lifshitz transitions. STM set-up conditions are: $I_{set} = 300$ pA, $V_{set} = -200$ mV (**a**); $I_{set} = 385$ pA, $V_{set} = 70$ mV (**b**); $I_{set} = 540$ pA, $V_{set} = 50$ mV (**c**); $I_{set} = 350$ pA, $V_{set} = 50$ mV (**d**).

$x \sim 0.17$ (Fig. 4c). To establish the mechanism of the mass formation and to understand its variation across the phase diagram, the next step is to image any mirror-symmetry-breaking distortion present in our samples.

In principle, STM images should be able to detect structural deformations. However, conventional low-bias topographies (Fig. 2c) showed only one of the two (either Pb/Sn or Se) sublattices, which is a square lattice with no detectable distortion³. In the present study, by systematically adjusting the imaging conditions²¹, we were able to detect both sublattices (Fig. 2d). We note here that, because STM measures the local density of states as well as the atomic corrugations²², one cannot always attribute periodic structures in STM topographies to atomic positions. In our case, by careful measurements of a series of bias-dependent topographies in multiple alloys of $Pb_{1-x}Sn_xSe$, we were able to establish that the low-bias topography shows the Se atoms whereas the higher-bias topographies show the Pb/Sn as well as the Se lattices (see Supplementary Discussion I for more details).

We now have sufficient information to look for signs of a mirror-symmetry-breaking distortion. Even though the higher-bias images exhibit a range of contrasts, we find that a distortion of the square lattice can be observed in local patches by eye. However, to explain the mass acquisition, we have to determine whether a long-range phase-coherent distortion exists in our sample. To establish this we create an average 4×4 -atom ‘supercell’^{23,24} (inset in Fig. 2c,d). The average unit cell clearly reveals a relative in-plane atomic shift between the two sublattices (Fig. 2a), resulting in a characteristic zigzag pattern (see Supplementary Discussion I for more details). This suggests that there is a single dominant domain within our field of view. This distortion, also known to occur within the bulk

of the endmember SnSe (ref. 25), breaks one of the two [110] mirror symmetries (Fig. 2a,b), leaving the other symmetry unaffected. To further substantiate the symmetry breaking observed in real space, we examine the two-dimensional Fourier transforms (FTs) of the STM topographs (Fig. 2e–j). The distortion observed should result in an effective broken C_4 symmetry when both sublattices are observed. We find that when only one sublattice is imaged at lower biases, the real parts of the Fourier components at the atomic Bragg peak wavevectors Q_x and Q_y have the same magnitude (Fig. 2e,i), whereas the respective imaginary parts are negligible (Fig. 2g), both consistent with the observed square lattice. We note that this also demonstrates the symmetry of our STM tip. Next, in STM topographs showing both sublattices acquired using the same STM tip, we find that an imaginary component emerges along exclusively one lattice direction (Q_y , but not Q_x). This corresponds to the C_4 symmetry breaking in the sample crystal structure (Fig. 2h,j), further confirming the long-range nature of the distortion. Our results present the first direct evidence for the generation of massive Dirac fermions out of the pool of their massless counterparts due to spontaneously broken crystal symmetry.

Next, we measure the magnitude of the distortion as a function of alloy composition. This would help us determine whether the decrease in the mass gap as we approach the critical concentration arises simply from a decrease in the magnitude of the observed distortion. Surprisingly we find that the magnitude of the structural distortion does not change significantly across the phase diagram (Fig. 4d), which implies that the mass variation occurs as a result of a different process. Our data suggest an alternative explanation for the Dirac gap variation, based on two factors: the broken crystal symmetry is present exclusively on the surface, and the surface state

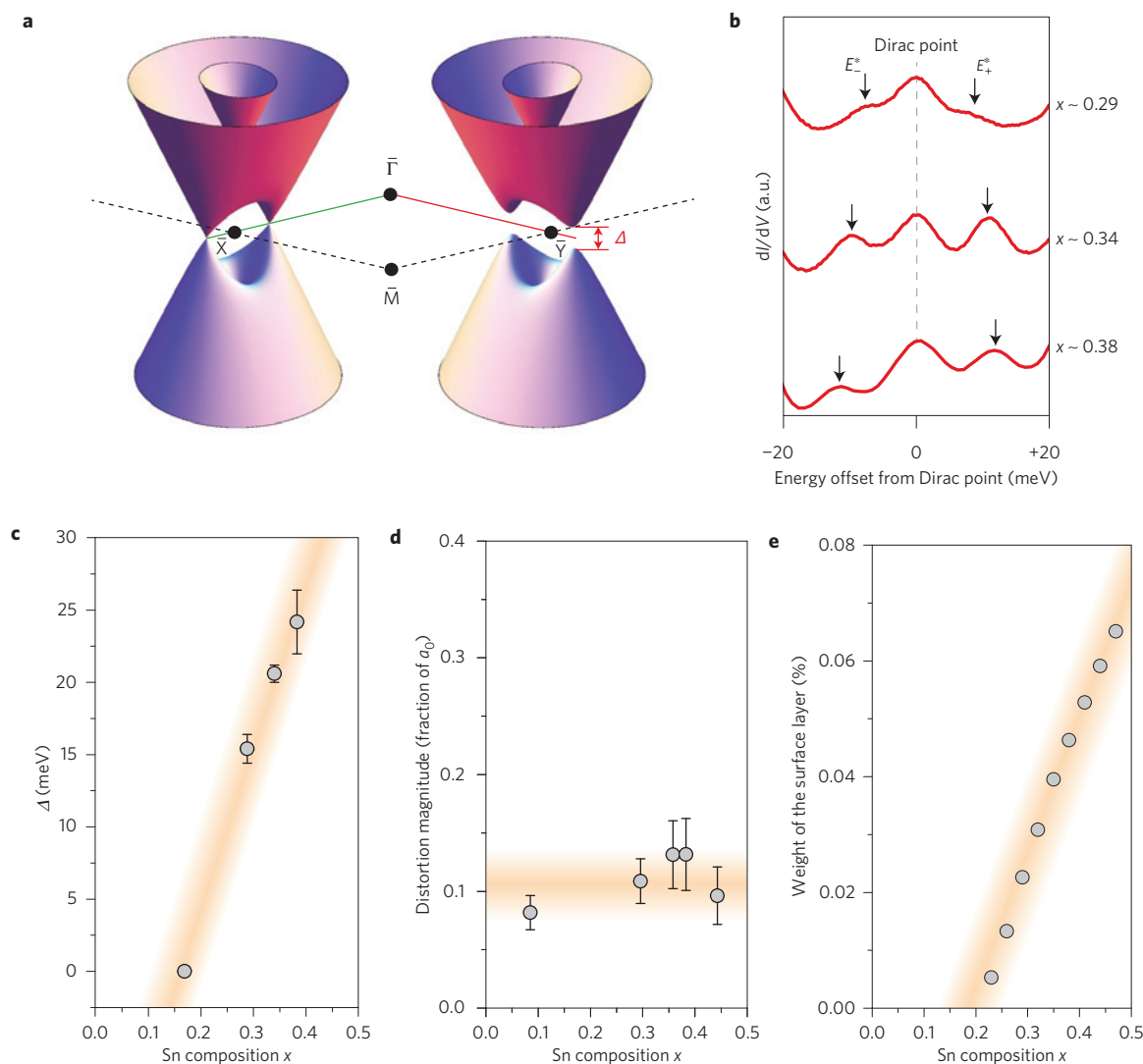


Figure 4 | Evolution of the Dirac gap with alloy composition. **a**, Illustration of the Dirac gap Δ opening in two out of the four Dirac cones within the first Brillouin zone owing to a broken $[\bar{1}10]$ mirror plane. **b**, Composition dependence of average dI/dV spectra acquired at 7.5 T, showing the evolution of the non-dispersing E^* LL peaks. **c**, Plot of Δ versus Sn composition, showing a monotonic increase in Δ in the topological regime. **d**, Magnitude of the distortion as a function of Sn composition, showing the presence of distortion of similar magnitude across a wide range of compositions (see Supplementary Discussion IV for more details). **e**, Theoretical calculations of the surface layer contribution to the Dirac wavefunction, showing a monotonic increase (penetration depth effectively decreases) with increased Sn doping. Orange lines in **c–e** represent guides for the eye. The width of the orange lines are for visualization purposes only. Vertical error bars in **c,d** are explained in Supplementary Discussions III and V, respectively.

penetration depth λ_{SS} increases on approaching x_c . In this scenario, the fraction of Dirac electrons sampling the broken-symmetry region decreases on approaching x_c , effectively ‘washing out’ the effect of the surface symmetry breaking, and thus creating a smaller Dirac mass.

To determine the validity of the scenario, we first determine whether the bulk is distorted. Our X-ray measurements in fact show a temperature-independent, bulk cubic structure, supporting the idea that the cubic symmetry is broken only at the surface (Fig. 1b). Let us now consider the second factor. According to theory, the weight of Dirac SS at the surface of a topological insulator is not a constant. An estimate for the length scale of the surface modes in the z -direction (perpendicular to the surface) is $\lambda_{SS} = \hbar v / E_g$, where v is the velocity of the Dirac fermions and E_g is the energy gap of the bulk states²⁶. This implies that if one could continuously tune the bulk bandgap, as the magnitude of the gap shrinks, the Dirac SS would penetrate progressively further into the bulk, ultimately penetrating the entire sample at the critical point when the bulk

gap closes. To quantitatively determine the surface weight of the SS as a function of composition, we use band structure parameters from our tight-binding model with varying Sn composition and calculate the percentage of the SS wavefunction in the topmost layer (Fig. 4e). Our calculations reveal that the SS weight on the top layer indeed decreases monotonically on approaching x_c , reflecting the penetration depth going to infinity near the quantum critical point. This, coupled with a distortion confined to the surface layers, is sufficient to explain our experimentally observed trend in the mass gap. In contrast, if we assume that the distortion persists within the bulk of the material, our calculations indicate that the gap would be nearly constant as a function of alloying content, which contradicts our experimental observations (Supplementary Information VI). Our experiments therefore indicate that the magnitude of the mass in our samples is controlled by the SS penetration into the bulk. Remarkably, our data represent the first observation of the striking effects of the divergent SS penetration depth on topological SS as the bulk approaches the critical concentration.

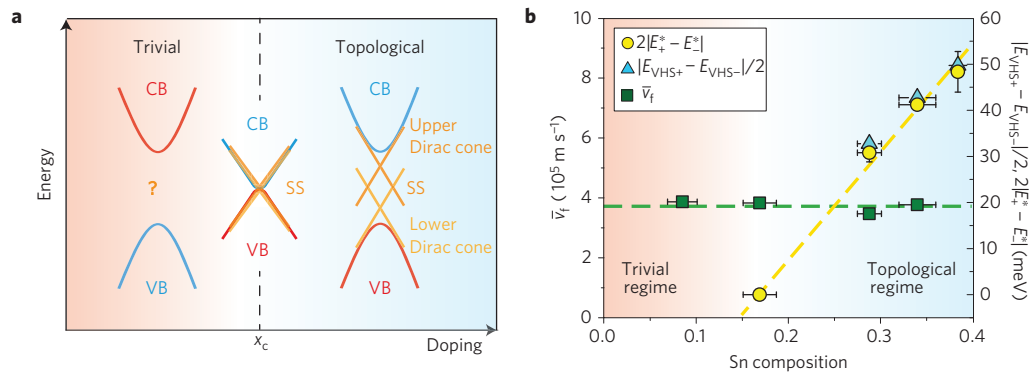


Figure 5 | Evolution of band structure with alloy composition. **a**, Schematic phase diagram of TCIs. The bandgap between the conduction (CB) and valence bands (VB) closes at a critical Sn concentration x_c of approximately 0.18 (ref. 14), causing band inversion and the formation of topologically protected SS consisting of two Dirac cones centred at each \bar{X} and \bar{Y} point. The question mark denotes one of the unknowns in the field regarding what surface states, if any, appear on the trivial side, and how they relate to their topological counterparts. **b**, Evolution of band structure parameters as a function of Sn composition. Average SS dispersion velocity \bar{v}_f assuming isotropic momentum dispersion, 2Δ and the energy of the Lifshitz transition are shown as green squares, yellow circles and blue triangles, respectively. Horizontal error bars denote the standard deviation in EDS measurements of Sn composition from five different areas of each sample. Vertical error bars are explained in Supplementary Discussion III.

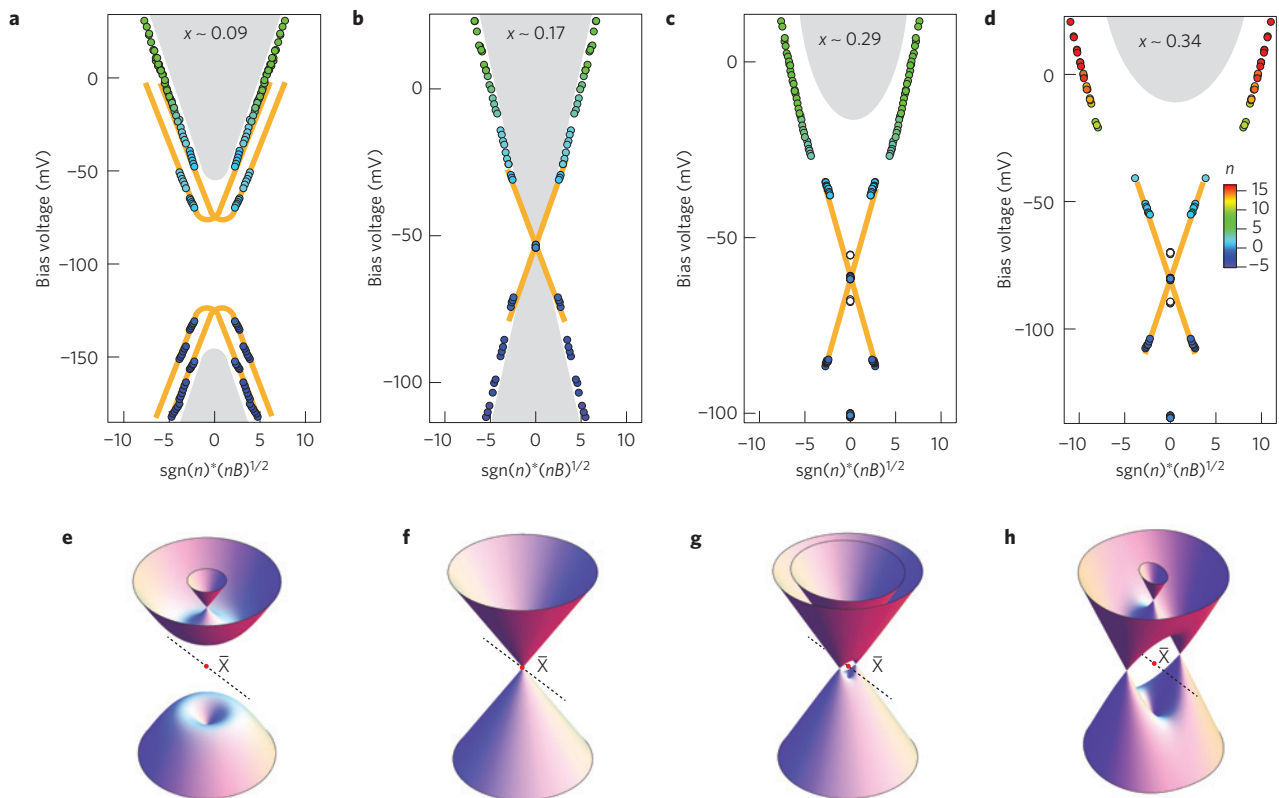


Figure 6 | Evolution of SS across the topological quantum phase transition. **a–d**, Plots of LL dispersion before **(a)**, at **(b)** and after **(c,d)** the topological transition. The double-branch dispersion in **a** shows the proximity state without the Dirac node, which is clearly observed in topological samples in **b–d**. Two Dirac cones are nearly indistinguishable in **b**, but become increasingly offset in energy with increasing Sn content **(c,d)**. Non-dispersing E^* peaks in **c,d** (white circles), are absent in the transition sample in **b**, which allows us to visualize the effect of composition changes on the Dirac gap, a property directly related to the Dirac fermion mass. Orange lines in **a–d** schematically depict the low-energy SS dispersions. Grey shaded regions indicate the positions of the bulk bands determined from ref. 14. Fits to the $\mathbf{k} \cdot \mathbf{p}$ model³⁴ are shown in Supplementary Discussion V. **e–h**, Illustrations of the SS band structure around the \bar{X} point in the absence of symmetry-breaking surface distortion, showing its evolution from the trivial to the topological regime. The absence of separate E_+^* and E_-^* peaks at the transition point $x \sim 0.17$ (Fig. 3b) suggests that Δ is approximately zero at this concentration.

Having understood the mechanism of mass acquisition, we turn to the evolution of the dispersion of SS across the critical composition, schematically portrayed in Fig. 5a. To extract the dispersion of the SS bands, we first need to index field-dispersing

LLs and plot them as a function of $(nB)^{0.5}$. As previously demonstrated³, this can be a non-trivial process owing to the complex band structure of topological SS involving multiple Dirac cones, which hybridize and go through a Lifshitz transition.

We determine the LL indices by using the $(nB)^{0.5}$ scaling behaviour to collapse the dispersion onto a continuous line. At the Lifshitz transition, the area of the constant energy contour changes rapidly, resulting in the van Hove singularities (VHS) observed in our dI/dV spectra (Fig. 3c,d) and a ‘jump’ in the LL indices¹³ (for example in Fig. 3g, the LL index jumps from $n = 1$ to $n = 3$). We begin with the LL plot of the topological sample at $x \sim 0.34$ (Fig. 6d), which reveals many of the features of the SS band structure, including the Lifshitz transitions schematically shown in Fig. 6h. In a sample with a lower Sn concentration ($x \sim 0.29$; Fig. 6c), we find that both the Dirac points of the upper and lower Dirac cones and VHS within each pair move closer to each other in energy than those in the $x \sim 0.34$ sample (Figs 5b and 6g), consistent with previous angle-resolved photoemission spectroscopy (ARPES) studies on a closely related TCI family^{27,28}. Following this trend, in the sample close to the transition point ($x \sim 0.17$), the SS almost completely overlap each other (within our resolution, we see only one), as schematically depicted in Fig. 5a. At this critical concentration, the V-shape of the dI/dV spectrum near the Dirac point disappears. Because the V-shape reflects the pure SS density of states far from the bulk bands, its absence suggests that the bulk gap at this concentration is close to zero, consistent with the critical point.

Finally, we turn our attention to the SS observed in the trivial phase below x_c (Fig. 3a,e). Using the same method of scaling as used for indexing the LLs of topological samples (Fig. 6b–d), we obtain a double-branched dispersion for both positive and negative LLs (Fig. 6a). Owing to the absence of a Dirac point and the double-branch dispersion, one might simply attribute these SS to conventional Rashba-split states, most notably known to occur on metal surfaces. However, the characteristics of the observed SS differ substantially from conventional Rashba states and should instead be viewed as topology-induced proximity states. In contrast to trivial surface states in metals, such as those occurring on Cu(111) or Au(111), which have two quadratic dispersions shifted in momentum space^{29,30}, both branches of our proximity SS exhibit linear dispersion away from the band bottom (coefficient of determination R^2 for the linear regression of all branches ~ 0.99) (Fig. 6a), with the dispersion velocity being constant (within $\sim 7\%$) in all samples (Fig. 5b). This indicates an intimate connection between SS in the topological and non-topological regimes.

These observations strongly suggest that the persistent SS in trivial TCIs are remnants of the nearby topological phase, rather than a simple consequence of the boundary conditions at the surface. Physically, the trivial SS can be understood in the following way. Like the topological SS, we start with two Dirac cones at the X point; however, when the bulk transitions into the trivial regime, the character of the SS changes such that mirror symmetry no longer protects the intersecting SS from being fully gapped out, leading to the trivial states shown in Fig. 6e. We note that the splitting of the two branches is $\sim 0.01 \text{ \AA}^{-1}$, which is at the border of momentum resolution of state-of-the-art laser ARPES studies, and could explain the inability to observe similar SS splitting^{31,32}. Our findings open up a new venue for characterizing and engineering highly tunable two-dimensional electron gases with novel properties. The highly symmetric nature and linear dispersion of the proximity SS bands and the large gap could potentially be exploited in constructing a new generation of electronics, based on Dirac SS. Furthermore, the geometric shape of these states inevitably creates a large density of states at the SS band edge, which could be used in realizing superconductivity in these systems if the Fermi level is tuned close to this energy by electrostatic gating³³. Finally, the topological SS that harbour both massive and massless Dirac fermions present a unique platform for future applications, as they can be independently tuned via structural symmetry breaking and alloying composition.

Methods

$\text{Pb}_{1-x}\text{Sn}_x\text{Se}$ single crystals with various Sn concentrations were grown by a self-selecting vapour growth method, cleaved in ultrahigh vacuum at 77 K, and immediately inserted into the STM head, where they are held at 4 K. We determine the composition by performing energy-dispersive X-ray spectroscopy (EDS) on multiple spots on each sample and averaging the obtained values.

Received 18 July 2014; accepted 8 January 2015;
published online 16 February 2015

References

- Fu, L. Topological crystalline insulators. *Phys. Rev. Lett.* **106**, 106802 (2011).
- Hsieh, T. H. *et al.* Topological crystalline insulators in the SnTe material class. *Nature Commun.* **3**, 982 (2012).
- Okada, Y. *et al.* Observation of Dirac node formation and mass acquisition in a topological crystalline insulator. *Science* **341**, 1496–1499 (2013).
- Zeljkovic, I. *et al.* Mapping the unconventional orbital texture in topological crystalline insulators. *Nature Phys.* **10**, 572–577 (2014).
- Hsieh, D. *et al.* A topological Dirac insulator in a quantum spin Hall phase. *Nature* **452**, 970–974 (2008).
- Xia, Y. *et al.* Observation of a large-gap topological-insulator class with a single Dirac cone on the surface. *Nature Phys.* **5**, 398–402 (2009).
- Chen, Y. L. *et al.* Experimental realization of a three-dimensional topological insulator, Bi_2Te_3 . *Science* **325**, 178–181 (2009).
- Hsieh, D. *et al.* A tunable topological insulator in the spin helical Dirac transport regime. *Nature* **460**, 1101–1105 (2009).
- Roushan, P. *et al.* Topological surface states protected from backscattering by chiral spin texture. *Nature* **460**, 1106–1109 (2009).
- Fu, L., Kane, C. & Mele, E. Topological insulators in three dimensions. *Phys. Rev. Lett.* **98**, 106803 (2007).
- Qi, X.-L. & Zhang, S.-C. Topological insulators and superconductors. *Rev. Mod. Phys.* **83**, 1057–1110 (2011).
- Hasan, M. Z. & Kane, C. L. Colloquium: Topological insulators. *Rev. Mod. Phys.* **82**, 3045–3067 (2010).
- Serbyn, M. & Fu, L. Symmetry breaking and Landau quantization in topological crystalline insulators. *Phys. Rev. B* **90**, 035402 (2014).
- Dziawa, P. *et al.* Topological crystalline insulator states in $\text{Pb}_{1-x}\text{Sn}_x\text{Se}$. *Nature Mater.* **11**, 1023–1027 (2012).
- Xu, S.-Y. *et al.* Observation of a topological crystalline insulator phase and topological phase transition in $\text{Pb}_{1-x}\text{Sn}_x\text{Te}$. *Nature Commun.* **3**, 1192 (2012).
- Hashimoto, K. *et al.* Quantum Hall transition in real space: From localized to extended states. *Phys. Rev. Lett.* **101**, 256802 (2008).
- Li, G. & Andrei, E. Y. Observation of Landau levels of Dirac fermions in graphite. *Nature Phys.* **3**, 623–627 (2007).
- Hanaguri, T., Igarashi, K., Kawamura, M., Takagi, H. & Sasagawa, T. Momentum-resolved Landau-level spectroscopy of Dirac surface state in Bi_2Se_3 . *Phys. Rev. B* **82**, 081305 (2010).
- Soumyanarayanan, A. *et al.* Imaging the nanoscale band structure of topological Sb. Preprint at <http://arxiv.org/abs/1311.1758> (2013).
- Agnihotri, O. P., Jain, A. K. & Gupta, B. K. X-ray investigations on Bridgman-grown $\text{Pb}_{1-x}\text{Sn}_x\text{Te}$ single crystals. *Mater. Sci. Eng.* **38**, 33–34 (1979).
- Gyenis, A. *et al.* Quasiparticle interference on the surface of the topological crystalline insulator $\text{Pb}_{1-x}\text{Sn}_x\text{Se}$. *Phys. Rev. B* **88**, 125414 (2013).
- Klijn, J. *et al.* STM measurements on the InAs(110) surface directly compared with surface electronic structure calculations. *Phys. Rev. B* **68**, 205327 (2003).
- Lawler, M. J. *et al.* Intra-unit-cell electronic nematicity of the high- T_c copper-oxide pseudogap states. *Nature* **466**, 347–351 (2010).
- Zeljkovic, I. *et al.* Scanning tunnelling microscopy imaging of symmetry-breaking structural distortion in the bismuth-based cuprate superconductors. *Nature Mater.* **11**, 585–589 (2012).
- Snykers, M., Delavignette, P. & Amelinckx, S. The domain structure of GeTe as observed by electron microscopy. *Mater. Res. Bull.* **7**, 831–839 (1972).
- Linder, J., Yokoyama, T. & Sudbø, A. Anomalous finite size effects on surface states in the topological insulator Bi_2Se_3 . *Phys. Rev. B* **80**, 205401 (2009).
- Tanaka, Y. *et al.* Experimental realization of a topological crystalline insulator in SnTe. *Nature Phys.* **8**, 800–803 (2012).
- Tanaka, Y. *et al.* Tunability of the k -space location of the Dirac cones in the topological crystalline insulator $\text{Pb}_{1-x}\text{Sn}_x\text{Te}$. *Phys. Rev. B* **87**, 155105 (2013).
- Hoesch, M. *et al.* Spin structure of the Shockley surface state on Au(111). *Phys. Rev. B* **69**, 241401 (2004).
- LaShell, S., McDougall, B. & Jensen, E. Spin splitting of an Au(111) surface state band observed with angle resolved photoelectron spectroscopy. *Phys. Rev. Lett.* **77**, 3419–3422 (1996).

31. Wojek, B. *et al.* Spin-polarized (001) surface states of the topological crystalline insulator $\text{Pb}_{0.73}\text{Sn}_{0.27}\text{Se}$. *Phys. Rev. B* **87**, 115106 (2013).
32. Yan, C. *et al.* Experimental observation of Dirac-like surface states and topological phase transition in $\text{Pb}_{1-x}\text{Sn}_x\text{Te}$ (111) films. *Phys. Rev. Lett.* **112**, 186801 (2014).
33. Goldstein, G., Aron, C. & Chamon, C. Band-edge superconductivity. Preprint at <http://arxiv.org/abs/1410.6103> (2014).
34. Liu, J., Duan, W. & Fu, L. Two types of surface states in topological crystalline insulators. *Phys. Rev. B* **88**, 241303 (2013).

Acknowledgements

We thank R. Buczko, C. Chamon, J. C. Seamus Davis, M. El-Batanouny, A. Mesaros, Y. Ran and A. Soumyanarayanan for useful conversations and G. McMahon for help with EDS measurements. V.M. gratefully acknowledges funding from the US Department of Energy, Scanned Probe Division under Award Number DE-FG02-12ER46880 for the support of I.Z., Y.O., W.Z. and D.W. for this project. Work at Massachusetts Institute of Technology is supported by US Department of Energy, Office of Basic Energy Sciences, Division of Materials Sciences and Engineering under Award DE-SC0010526 (L.F.), and NSF-DMR-1104498 (M.S.). H.L. acknowledges the Singapore National Research Foundation for support under NRF Award No. NRF-NRFF2013-03. Y.O. was partly supported by JSPS KAKENHI Grant Numbers 26707016 and 00707656. The work at Northeastern University is supported by the US Department of Energy grant number DE-FG02-07ER46352, and benefited from Northeastern University's Advanced Scientific

Computation Center (ASCC), theory support at the Advanced Light Source, Berkeley and the allocation of supercomputer time at the NERSC through DOE grant number DE-AC02-05CH11231. Work at Princeton University is supported by the US National Science Foundation Grant, NSF-DMR-1006492. F.C. acknowledges the support provided by MOST-Taiwan under project number NSC-102-2119-M-002-004.

Author contributions

Y.O. and I.Z. contributed equally to this work. Y.O., I.Z. and V.M. designed the experiments. STM experiments were carried out by Y.O., I.Z., D.W. and W.Z. I.Z., Y.O., L.F. and V.M. analysed the data and wrote the paper. Samples were obtained from R.S., F.C. and M.Z.H. F.C. and R.S. contributed to the single-crystal growth and structural analysis. L.F. conceived the theoretical explanation for this work. M.S. performed analytical model calculations. H.L. and A.B. supervised the first-principles part of the work, which was performed by G.C., Y.J.W., J.L. and H.L.

Additional information

Supplementary information is available in the [online version of the paper](#). Reprints and permissions information is available online at www.nature.com/reprints. Correspondence and requests for materials should be addressed to V.M.

Competing financial interests

The authors declare no competing financial interests.